Data-Enabled Predictive Control and Guidance for Autonomous Underwater Vehicles

Sebastian Zieglmeier * Mathias Hudoba de Badyn * Narada D. Warakagoda ** Thomas R. Krogstad ** Paal Engelstad *

* Department of Technology Systems, University of Oslo, 2027 Kjeller, Norway (e-mail: sebastiz, mathihud @uio.no)

Abstract: This paper presents a fully data-driven control framework for autonomous underwater vehicles (AUVs) based on Data-Enabled Predictive Control (DeePC). The approach eliminates the need for explicit hydrodynamic modeling by exploiting measured input—output data to predict and optimize future system behavior. Classic DeePC was employed in the heading control, while a cascaded DeePC architecture is proposed for depth regulation, incorporating a loop-frequency separation to handle the different dynamic modes of input and output. For 3-D waypoint path following, the Adaptive Line-of-Sight algorithm is extended to a predictive formulation and integrated with DeePC. All methods are validated in extensive simulation on the REMUS 100 AUV and compared with classical PI/PID control. The results demonstrate superior tracking performance and robustness of DeePC under ocean-current disturbances and nonlinear operating conditions, while significantly reducing modeling effort.

Keywords: Data-driven Model Predictive Control, Autonomous Underwater Vehicles, Cascaded DeePC, Predictive ALOS, 3-D path following.

1. INTRODUCTION

Autonomous Underwater Vehicles (AUVs) have become central to modern marine exploration, inspection, and defense activities (Gu et al., 2022). Ensuring reliable pathfollowing and trajectory tracking in such missions requires controllers that can cope with nonlinear hydrodynamics and environmental disturbances (Shen and Shi, 2020). These control objectives are typically achieved through a hierarchical control structure, which integrates a high-level guidance system responsible for generating appropriate reference signals, an intermediate-level controller tracking those references, and a low-level control system that directly manages the actuators (Breivik and Fossen, 2009). A classic example of a high-level guidance system for AUVs is Line-of-Sight (LOS) guidance. The LOS method provides a geometric three-point guidance rule for steering the vehicle toward a target point on the desired path, effectively translating the spatial error into a heading command (Breivik and Fossen, 2009; Børhaug and Pettersen, 2006). More sophisticated LOS-based guidance laws have been summarized in (Gu et al., 2022), and the state-of-the-art lies in the Adaptive Line-of-Sight (ALOS) algorithm, which optimizes reference generation by compensating for varying environmental conditions (Fossen, 2023). In practice, these high-level guidance laws are commonly paired with reactive PI/PID controllers that do not account for future behavior or constraints. As a result, their performance deteriorates when faced with strong nonlinearities, actuator

saturation, or delays in dynamics. Consequently, predictive control strategies have been introduced to AUVs, such as Model Predictive Control (MPC) (Rout and Subudhi, 2020; Shen and Shi, 2020).

These approaches require a model of the AUV dynamics, which is complex and time-consuming (Taubert et al., 2014). The hydrodynamic coefficients that characterize added mass, drag, lift, and damping are often nonlinear, coupled, and highly dependent on factors such as vehicle geometry, speed, and surrounding flow conditions. Identifying these parameters requires extensive experiments that are time-consuming and context-specific (Taubert et al., 2014), and the resulting models typically remain valid only within a limited operating range, reducing their applicability across different speeds, payloads, or environmental conditions. Such challenges have motivated data-driven control approaches, which exploit measured data to design and execute control laws without requiring an explicit parametric model of the system. Within this context, the Data-Enabled Predictive Control (DeePC) framework introduced in (Coulson et al., 2019) has emerged as one of the most promising approaches. DeePC uses offline trajectories of inputs and outputs to solve a constrained optimization problem for optimal control inputs. This is particularly attractive for AUV applications, especially due to its potential to also handle complex and nonlinear dynamics (Elokda et al., 2021).

This work focuses on employing DeePC in an AUV for path-following with the following contributions:

^{**} Norwegian Defence Research Establishment, 2027 Kjeller, Norway

^{*} Code available: https://github.com/SebsDevLab/DeePC_AUV.git

- Implementation and integration of DeePC within the heading control autopilot.
- Design of a cascaded DeePC-based depth control architecture.
- Extension of the ALOS guidance algorithm into a predictive adaptive line-of-sight (PALOS) formulation, allowing integration with the DeePC-based tracking controllers.

This paper is organized as follows. Notation is outlined in Section 2, and the general AUV dynamics, state-of-theart, and theoretical foundations of DeePC are in Section 3, Section 4, and Section 5, respectively. Subsequently, the control architecture design and PALOS are described in Section 6-7, and numerical results obtained from detailed MSS-based simulations (Fossen and Perez, 2004) are analyzed in Section 8. Additionally, the study includes stress tests addressing system nonlinearities and ocean currents to evaluate the robustness and identify the limitations of the proposed control approaches. The built-in PID controllers and the ALOS algorithm from the MSS toolbox are employed as benchmarks to contextualize the obtained results. Finally, the conclusion and future works are in Section 9.

2. NOTATION

 $x_k \in \mathbb{R}^n$ denotes the value of x at the discrete time step k, where \mathbb{R} denotes the set of real numbers and nthe dimension. The operator $diag\{x\}$ denotes a diagonal matrix whose diagonal entries are given by the elements of the vector x.

 $||x||_M^2$ denotes the squared weighted euclidean norm of the vector x with the positive weighting matrix M, where $||x||_M^2 := x^\top M x$. The stacked column vector of a sequence $\{x\}_a^b$ is denoted as $x := \begin{bmatrix} x_a^\top ... x_b^\top \end{bmatrix}^\top$. The position coordinates of the AUV in the NED frame are

denoted by x_p, y_p, z_p , where the subscript p is introduced to avoid confusion with the conventional control-system state x and output y.

3. AUTONOMOUS UNDERWATER VEHICLE

The AUV considered in this study is the REMUS 100, as implemented in Fossen's MSS toolbox (Fossen and Perez, 2004). The model includes six degrees of freedom (6-DOF) dynamics with actuation provided by a threebladed propeller, stern, and rudder fins, allowing control of surge, heave, and sway motions. The REMUS 100 is a representative small vehicle with a weight of approximately 31.9 kg, a length of 1.6 m, and a diameter of 0.19 m. (Fossen, 2021) provides a detailed presentation of the mathematical models and theoretical concepts underlying longitudinal AUVs. In this paper, only the main relations relevant for control design are summarized, while the specific REMUS 100 parameters are obtained from the MSS toolbox (Fossen and Perez, 2004). Appendices B–D provide the explicit dynamic formulations and supplementary material supporting the subsequent derivations.

3.1 The rigid-body equations of an AUV

The dynamics of the AUV are represented using a standard 6-DOF rigid-body formulation (Fossen, 2021). The vehicle state $x = [\eta^{\top}, \nu^{\top}]^{\top}$ is defined by its pose η and velocity vector ν . The pose consists of its position x_p, y_p, z_p in the inertial NED frame and the attitude, consisting of the Euler angles ϕ, θ, ψ , which describe the orientation of the body frame relative to the NED frame in (1). The linear velocities u, v, w (surge, sway, heave) and angular velocities p, q, r (roll, pitch, yaw) in the velocity vector ν are expressed in the body frame given in (2). The relative velocity with respect to the surrounding water is given in (3), where $\nu_c = [u_c, v_c, w_c, 0, 0, 0]^{\top}$ contains the ocean currents expressed in the body frame.

$$\eta = [x_p, y_p, z_p, \phi, \theta, \psi]^{\top} \in \mathbb{R}^6, \tag{1}$$

$$\eta = [x_p, y_p, z_p, \phi, \theta, \psi]^{\top} \in \mathbb{R}^6,$$

$$\nu = [u, v, w, p, q, r]^{\top} \in \mathbb{R}^6,$$
(2)

$$\nu_r = \nu - \nu_c,\tag{3}$$

The kinematic relation in (4) describes the vehicle motion in the inertial NED frame and depends on the absolute body-fixed velocity ν . In contrast, the dynamic model in (5) is expressed in terms of the relative velocity ν_r , since the hydrodynamic forces depend on the motion of the vehicle relative to the surrounding water.

$$\dot{\eta} = J(\eta)\nu\tag{4}$$

$$M\dot{\nu}_r + C(\nu_r)\nu_r + D(\nu_r)\nu_r + g(\eta) = \tau + \tau_{LD} + \tau_{CF}$$
 (5)

3.2 AUV dynamic matrices

The detailed derivation of the describing dynamic components of the AUV is attached in Appendix B and C. The kinematic equation, given in (4), is defined by the transformation matrix $J(\eta)$, mapping body-fixed linear and angular velocities to the time derivatives of the vehicle's position and orientation in the NED frame. The inertia matrix M of the AUV is composed of the rigidbody inertia M_{RB} , depending on the vehicle's mass properties, and the added-mass matrix M_A , depending on the hydrodynamic contribution caused by the acceleration of the surrounding fluid. In the MSS toolbox, M_A is assumed constant, resulting in a constant M as in (6).

$$M = \begin{bmatrix} m_{11} & 0 & 0 & m_{15} & 0 \\ 0 & m_{22} & 0 & m_{24} & 0 & 0 \\ 0 & 0 & m_{33} & 0 & 0 & 0 \\ 0 & m_{42} & 0 & m_{44} & 0 & 0 \\ m_{51} & 0 & 0 & 0 & m_{55} & 0 \\ 0 & 0 & 0 & 0 & 0 & m_{66} \end{bmatrix}.$$
 (6)

The Coriolis-centripetal matrix $C(\nu_r)$ in (7) represents gyroscopic and cross-coupling effects arising from linear and angular motion. It is composed of the rigid-body term $C_{RB}(\nu_r)$, depending on the angular velocities in ν_r , and the added-mass term $C_A(\nu_r)$, depending on the relative linear velocities in ν_r . Both dependencies contribute to the nonlinear character of the AUV dynamics.

$$C(\nu_r) = C_{RB}(\nu_r) + C_A(\nu_r). \tag{7}$$

The damping matrix $D(\nu_r)$ is modeled as a diagonal matrix, representing damping in each degree of freedom with the damping coefficients $X_u, Y_v, Z_w, K_p, M_q, N_r$. To account for nonlinear effects at higher speeds, the damping in the surge and sway directions decreases in the RE-MUS 100 simulation exponentially with the total relative velocity U_r , introducing velocity-dependent behavior in the damping matrix. The resulting formulation is

$$D(\nu_r) = -\operatorname{diag}\left\{ X_u e^{-3U_r}, \ Y_v e^{-3U_r}, \ Z_w, \ K_p, \ M_q, \ N_r \right\}.$$
 (8)

The vector $g(\eta)$ represents the restoring forces and moments acting on the vehicle due to gravity and buoyancy, resulting in nonlinear attitude-dependent behavior. For neutrally buoyant underwater vehicles such as the RE-MUS 100, these effects are primarily determined by the position of the center of gravity, defined as $r_{bG} = [x_g, y_g, z_g]^T$ and the gravitational force mg, relative to the body-fixed origin as in (9).

$$g(\eta) = \begin{bmatrix} \mathbf{0}_{3\times1} \\ z_{g}mg\cos(\theta)\sin(\phi) - y_{g}mg\cos(\theta)\cos(\phi) \\ z_{g}mg\sin(\theta) + x_{g}mg\cos(\theta)\cos(\phi) \\ x_{g}mg\cos(\theta)\sin(\phi) - y_{g}mg\sin(\theta) \end{bmatrix}$$
(9)

3.3 AUV Forces and Moments

The control input vector is defined as $u = [\delta_s, \delta_r, n_p]^{\top}$, where δ_s and δ_r denote the stern and rudder plane deflections, and n_p denotes the propeller speed. These inputs generate the generalized forces and moments τ acting on the AUV. In particular, τ results from the lift and drag forces produced by the stern and rudder planes, i.e., X_s, X_r, Y_r, Z_s , together with the propeller thrust X_{prop} and torque K_{prop} . The resulting generalized force vector is given in (10), where x_r, x_s are the longitudinal positions of the rudder and stern planes relative to the body-fixed origin.

$$\tau = [X_{\text{prop}} + X_r + X_s, Y_r, Z_s, K_{\text{prop}}, -x_s Z_s, x_r Y_r]^{\top}$$
 (10) The lift–drag vector τ_{LD} in (11) consists of the longitudinal and vertical components $\tau_{LD,X}$ and $\tau_{LD,Z}$, which represent the combined lift and drag forces expressed in the body-fixed frame.

$$\tau_{LD} = [\tau_{LD,X}, 0, \tau_{LD,Z}, 0, 0, 0]^{\top}$$
(11)

The total generalized cross-flow drag vector acting on the vehicle is given in (12), representing the hydrodynamic forces and moments in sway, heave, pitch, and yaw due to lateral and vertical flow separation along the hull.

$$\tau_{CF} = [0, Y_{CF}, Z_{CF}, 0, M_{CF}, N_{CF}]^{\top},$$
 (12)

3.4 Ocean current dynamics

Ocean currents are modeled as irrotational, such that only the linear velocity components contribute to the relative motion between the AUV and the surrounding water. The current in the NED frame is decomposed into a horizontal component with magnitude V_c and direction β_c , and a vertical component W_c ,

$$\nu_c^n = \left[V_c \cos(\beta_c), \ V_c \sin(\beta_c), \ W_c \right]^\top. \tag{13}$$

Further in-depth modeling details are provided in Appendix D.

4. CLASSIC AUV CONTROL

Since the control objective of this work is path-following, the propeller speed n_p is fixed to a constant value corresponding to a nominal cruising velocity. The controller gains of the following PI/PID controllers were tuned by pole placement as described in (Fossen, 2021) and (Beard and McLain, 2012).

4.1 Heading Control

The heading control loop (upper loop in Fig. 1) employs a low-pass (LP) filter to generate a smooth desired yaw

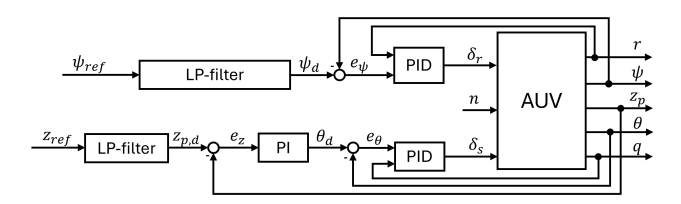


Fig. 1. Classic AUV control architecture with the PID heading control and the cascaded PI/PID control of the heave position with an inner loop controlling the pitch angle.

angle ψ_d from the commanded heading ψ_{ref} . Using in addition the measured yaw angle ψ and yaw rate r, the rudder input δ_r is computed by a PID controller according to (14).

$$\delta_r = -K_{p_{\psi}}(\psi - \psi_d) - K_{d_{\psi}}r - K_{i_{\psi}} \int_0^t (\psi - \psi_d) \,d\tau.$$
 (14)

4.2 Depth Control

The depth control loop (lower loop in Fig. 1) employs a cascaded structure. An LP filter smooths the reference $z_{\rm ref}$ to a desired heave position $z_{p,d}$. The outer PI controller generates a desired pitch angle θ_d from the depth error $e_z = z_p - z_{p,d}$, while the inner PID controller regulates θ with the pitch rate q via the stern-plane deflection δ_s :

$$\theta_{d} = K_{p_{z}}(z_{p} - z_{p,d}) + K_{i_{z}} \int_{0}^{t} (z_{p} - z_{p,d}) d\tau,
\delta_{s} = -K_{p_{\theta}}(\theta - \theta_{d}) - K_{d_{\theta}} q - K_{i_{\theta}} \int_{0}^{t} (\theta - \theta_{d}) d\tau.$$
(15)

4.3 Adaptive Line-of-Sight Guidance Law

The ALOS guidance law (Fossen and Aguiar, 2024) provides a 3-D formulation for path following of AUVs. It generates desired yaw and pitch angles, ψ_d and θ_d , to align the vehicle with a spatial path while adaptively compensating for unknown constant disturbances such as ocean currents. The spatial path is described by the position vector $p_s(s) = [x_s(s), y_s(s), z_s(s)]^{\top}$, parameterized by the path variable s and contains all possible points on the path. This representation can encode smooth curves, splines, or straight lines. Its local orientation is given by the tangent vector $t_t(s)$, which in this work is simplified to a straight line between two consecutive waypoints as in (16).

$$t_t(s) = \begin{bmatrix} x_t' \\ y_t' \\ z_t' \end{bmatrix} = \begin{bmatrix} x_{wp,k+1} - x_{wp,k} \\ y_{wp,k+1} - y_{wp,k} \\ z_{wp,k+1} - z_{wp,k} \end{bmatrix}.$$
(16)

The resulting path heading and elevation angles, π_h and π_v , respectively, are computed as

$$\pi_h = \arctan\left(\frac{y_t'(s)}{x_t'(s)}\right), \pi_v = \arctan\left(\frac{-z_t'(s)}{\sqrt{x_t'(s)^2 + y_t'(s)^2}}\right). \quad (17)$$

The cross- and vertical-track errors in the path-tangential frame (superscript p) are computed by rotating the position error in the NED frame, $p_e^n = p - p_s$, using the standard rotation matrices $R_z(\pi_h)$ and $R_y(\pi_v)$ about the z- and y-axes, respectively, as shown in (18).

$$\begin{bmatrix} x_e^p \\ y_p^p \\ z_e^p \end{bmatrix} = \begin{bmatrix} \cos \pi_v & 0 & \sin \pi_v \\ 0 & 1 & 0 \\ -\sin \pi_v & 0 & \cos \pi_v \end{bmatrix}^\top \begin{bmatrix} \cos \pi_h & -\sin \pi_h & 0 \\ \sin \pi_h & \cos \pi_h & 0 \\ 0 & 0 & 1 \end{bmatrix}^\top \begin{bmatrix} x_e^n \\ y_e^n \\ z_e^n \end{bmatrix}, (18)$$

To account for drift effects, the algorithm adapts horizontal and vertical crab angles, $\hat{\beta}_c$ and $\hat{\alpha}_c$, and commands

$$\psi_d = \pi_h - \hat{\beta}_c - \arctan\left(\frac{y_e^p}{\Delta_h}\right), \theta_d = \pi_v + \hat{\alpha}_c + \arctan\left(\frac{z_e^p}{\Delta_v}\right),$$
(19)

where Δ_h and Δ_v denote the horizontal and vertical look-ahead distances. To ensure smooth and dynamically feasible reference signals, the raw LOS angles ψ_d and θ_d generated by the ALOS law are filtered through a discrettime LOS observer, which estimates both the filtered LOS angles and their corresponding rate commands (r_d, q_d) . The procedure suppresses discontinuities introduced by waypoint transitions and provides differentiable reference trajectories for the inner control loops. The adaptive update laws for the estimated drift angles in ALOS are expressed as,

$$\dot{\hat{\beta}}_c = \frac{\gamma_h y_e^p \Delta_h}{\sqrt{\Delta_h^2 + (y_e^p)^2}}, \qquad \dot{\hat{\alpha}}_c = \frac{\gamma_v z_e^p \Delta_v}{\sqrt{\Delta_v^2 + (z_e^p)^2}}, \qquad (20)$$

with positive adaptation gains $\gamma_h, \gamma_v > 0$, ensuring uniform semiglobal exponential stability of the cross-track errors for straight-line path following (Fossen and Aguiar, 2024).

5. DATA-ENABLED PREDICTIVE CONTROL

The DeePC framework, introduced in (Coulson et al., 2019), relies on measured input–output trajectories that are sufficiently informative to capture the system dynamics, a property known as persistency of excitation (Willems et al., 2005). According to Willems' Fundamental Lemma, any trajectory of a controllable and observable LTI system can be expressed as a linear combination of previously recorded input–output data. The collected input and output sequences, $u_{\rm data}$ and $y_{\rm data}$, are arranged into block Hankel matrices $\mathcal{H}(u)$ and $\mathcal{H}(y)$ with r block rows and c columns, as defined in (Coulson et al., 2019). Alternatively, the data can be structured as a Page matrix $\mathcal{H}_P(u)$ as in (21), which groups consecutive columns into separate pages (Coulson et al., 2021).

$$\mathscr{H}(u) = \begin{bmatrix} u_1 & u_2 & \cdots & u_c \\ \vdots & \vdots & \cdots & \vdots \\ u_r & u_{r+1} & \cdots & u_{r+c-1} \end{bmatrix}, \mathscr{H}_P(u) = \begin{bmatrix} u_1 & u_{r+1} & \cdots & u_{(c-1)r+1} \\ \vdots & \vdots & \cdots & \vdots \\ u_r & u_{2r} & \cdots & u_{cr} \end{bmatrix}$$
(21)

General persistency of excitation requires these data matrices to be of full row rank (Coulson et al., 2019). For noisy data, a quantitative characterization of this condition was introduced in (Coulson et al., 2022), relating the degree of excitation to the singular value of the data matrix. For the DeePC formulation, the data matrices are partitioned into past and future components as in (22), where (U_p, Y_p) encode past trajectories for initialization, and (U_f, Y_f) define the future trajectories used for prediction.

$$U_d = \begin{bmatrix} U_p \\ U_f \end{bmatrix}, \qquad Y_d = \begin{bmatrix} Y_p \\ Y_f \end{bmatrix} \tag{22}$$

Consider a discrete-time system with inputs $u \in \mathbb{R}^m$ and outputs $y \in \mathbb{R}^p$ over a prediction horizon N. Let u_{ini} and y_{ini} denote the past input-output trajectories of length T_{ini} , and u and y the future control inputs and predicted outputs, respectively. The DeePC framework formulates the following finite-horizon optimization problem:

$$\begin{aligned} & \underset{g,u,y,\sigma}{\min} & \|r-y\|_Q^2 + \|u\|_R^2 + \|g\|_{\lambda_g}^2 + \|\sigma_y\|_{\lambda_y}^2 \\ & \text{s.t.} & \begin{pmatrix} U_p \\ Y_p \\ U_f \\ Y_f \end{pmatrix} g = \begin{pmatrix} u_{\text{ini}} \\ y_{\text{ini}} \\ u \\ y \end{pmatrix} + \begin{pmatrix} 0 \\ \sigma_y \\ 0 \\ 0 \end{pmatrix}, \\ & u_{\text{min}} \leq u \leq u_{\text{max}}, \\ & y_{\text{min}} \leq y \leq y_{\text{max}}, \\ & u_k \in \mathcal{U}, \ y_k \in \mathcal{Y}, \quad \forall k \in \{0,\dots,N-1\}. \end{aligned}$$
 Here, $g \in \mathbb{R}^{T-T_{\text{ini}}-N+1}$ is the decision vector that lin-

Here, $g \in \mathbb{R}^{T-T_{\mathrm{ini}}-N+1}$ is the decision vector that linearly combines past trajectories to reconstruct the system behavior, and $r \in \mathbb{R}^p$ denotes the reference trajectory. $Q \in \mathbb{R}^{p \times p}$ and $R \in \mathbb{R}^m \times^m$ are positive definite weighting matrices. The regularization terms $\|g\|_{\lambda_g}^2$ and $\|\sigma_y\|_{\lambda_y}^2$, with $\lambda_g, \lambda_y > 0$, follow the approach of (Huang et al., 2023) to improve robustness against measurement noise and nonlinearities. Input and output constraints are directly incorporated through the box constraints and admissible sets $\mathcal U$ and $\mathcal Y$. Theoretical and experimental guarantees regarding robustness and stability are provided in (Berberich et al., 2020, 2021; Berberich and Allgöwer, 2024).

6. DEEPC FOR AUV

A fully coupled DeePC formulation incorporating all three control inputs and twelve states could, in principle, capture the complete 6-DOF dynamics of the AUV, provided that sufficiently rich data persistently excite all relevant dynamic modes. However, the dynamics of the different states operate in different frequency regimes, and exhibit distinct damping behavior, which makes a fully coupled formulation unsuitable for AUV control. Consequently, this work adopts a decoupled control architecture, consistent with classical AUV control principles, comprising independent heading and depth control loops, as illustrated in Fig. 2.

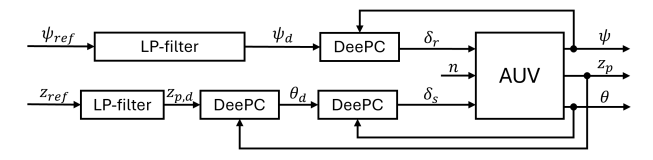


Fig. 2. Control architecture of the DeePC-based heading control and the cascaded DeePC control of the heave position with an inner loop controlling the pitch angle.

6.1 DeePC Heading Control

For a direct performance comparison, the DeePC-based heading control employs the same LP reference filter as the classical PID structure. To generate a predictive reference trajectory over the control horizon $T_{\rm fut}$, a predictive LP filter computes the next $T_{\rm fut}$ samples of the desired yaw angle ψ_d from the commanded reference $\psi_{\rm ref}$. At each control step, DeePC determines the optimal sequence of rudder deflections δ_r over the prediction horizon by minimizing the objective function defined in (23). Only the first control action is applied to the system, after which the resulting yaw angle ψ is measured. The applied control input δ_r and the measured output ψ are then appended to the vectors $u_{{\rm past},\delta_r}$ and $y_{{\rm past},\psi}$, which are required to estimate the current system state through a linear combination of previously collected trajectories. This offline dataset

used for constructing the data matrices U_d and Y_d was generated in the REMUS 100 AUV simulator by exciting the rudder input δ_r with a chirp signal overlaid with a pseudo-random binary sequence (PRBS), while recording the corresponding yaw response ψ . Since both signals operate within the same dynamic mode, the resulting dataset is sufficiently rich and satisfies the persistency-of-excitation condition. To capture a larger number of data points and therefore extend the operational range represented in the data, the Page matrix, given in (21), was adopted instead of the Hankel matrix. This receding-horizon loop is then executed iteratively throughout the control process.

6.2 DeePC Depth Control

To integrate DeePC into the depth control, two possible control architectures can be considered. The first approach directly maps the stern-plane deflection δ_s to the heave position z_p . However, since the depth response of an AUV exhibits significantly slower dynamics compared to the control input δ_s , the system effectively behaves as a strong LP filter. This leads to two major issues: obtaining persistently exciting data becomes difficult due to the limited dynamic coupling between input and output, and reducing the control frequency to be able to collect sufficiently rich data may cause higher-frequency disturbances to remain unregulated. Therefore, a cascaded DeePC structure, analogous to the classical depth control scheme, is adopted. In this configuration, the outer DeePC maps the desired heave position z_d to a desired pitch angle θ_d , while the inner DeePC regulates θ_d through the stern-plane deflection δ_s . The inner loop design closely follows the heading control formulation discussed previously. Due to the cascaded DeePC structure, the two control loops operate at different frequencies, with the inner loop running $r_f = f_{\text{inner}}/f_{\text{outer}}$ times faster than the outer loop. This allows the inner DeePC to compensate for disturbances with faster dynamics, while the outer loop tracks the heave position trajectory. Because the pitch dynamics lie between the fast dynamics of δ_s and the slow depth dynamics, this cascaded structure ensures both sufficient excitation and improved robustness.

While the data collection process for the inner loop is straightforward as for the heading control, collecting suitable data for the outer loop requires additional consideration, as its effective plant consists of the inner DeePC controller combined with the AUV dynamics. At first glance, this appears incompatible with the DeePC framework, as the inner DeePC involves an embedded optimization, breaking the deterministic LTI structure typically assumed by Willems' Fundamental Lemma. To overcome this, a perfect control assumption, analogous to the unity-gain property in cascaded PID control (Beard and McLain, 2012), is introduced. This idealized condition assumes that the inner loop perfectly tracks its reference, i.e., $\theta = \theta_d$, thereby allowing the pitch angle θ to be used as the effective input and the measured heave position z_n as the output for the outer-loop data sequences.

Two different strategies can be employed here for collecting this data. A more direct approach is to subsample θ and z_p every r_f -th step from the inner-loop dataset to form the outer-loop dataset. However, this approach complicates the construction of an input excitation δ_s that sufficiently covers both the pitch dynamics for the inner

loop and the depth dynamics for the outer loop over both their full ranges. Therefore, a two-stage data-collection procedure is preferred. After collecting the data sequences for the inner loop, these are directly employed in the inner DeePC loop during the outer-loop data collection. In this configuration, a θ_d -chirp signal with an overlaid PRBS, based on the slower outer-loop frequency, can be applied to ensure that both θ and z_p exhibit dynamic coupling and persistently exciting behavior across their respective dynamic ranges. These data sequences are stored in the Page matrix format to cover a bigger operational range.

During control execution, the inner DeePC loop operates at the frequency $f_{\rm inner}$, which matches the AUV's simulation and sampling frequency, while the outer loop runs at the lower frequency $f_{\rm outer}$. Consequently, the measurements of θ and z_p are also available at every k-th time step. When the outer loop is executed at time step k, the predictive LP filter generates the desired heave position trajectory

$$z_d[k + r_f, k + 2r_f, \dots, k + (T_{\text{fut}} - 1)r_f]$$

which serves as the reference trajectory for the outer DeePC optimization. The historical data vectors $u_{\text{past},\theta}$ and y_{past,z_p} contain the most recent T_{ini} samples corresponding to

$$z[k-1-(T_{\text{ini}}-1)r_f, \ldots, k-1-r_f, k-1],$$

 $\theta[k-1-(T_{\text{ini}}-1)r_f, \ldots, k-1-r_f, k-1],$

as illustrated in Fig. 3 by the red dots. The outer-loop optimization then predicts the desired pitch sequence (upper black dots)

$$\theta_d[k + r_f, k + 2r_f, \dots, k + (T_{\text{fut}} - 1)r_f]$$
.

After solving the optimization problem, only the first element $\theta_d[k+r_f]$ is applied as the desired command for the inner loop. Two methods can be used to propagate θ_d between successive updates of the outer loop. The first employs a zero-order hold, maintaining $\theta_d[k+r_f]$ constant over the next r_f inner-loop iterations. While straightforward, this approach introduces discontinuities in θ_d at each outer-loop update, resulting in slightly oscillatory stern-plane commands. A more refined and recommended approach linearly interpolates θ_d between the current value $\theta_d[k]$ and the next update $\theta_d[k+r_f]$, ensuring smooth transitions and reducing control jitter. To ensure that all innerloop DeePC optimizations have access to a continuous reference, the interpolated θ_d sequence is extrapolated up to $k + r_f + T_{\text{fut,inner}}$ as illustrated in Fig. 3 by the pink dashed line. The inner DeePC loop then tracks this continuously updated θ_d using the same structure classically.

7. 3-D PATH FOLLOWING WITH DEEPC

To achieve 3-D waypoint tracking with DeePC, the ALOS guidance law is integrated into the predictive control structure. Instead of providing only instantaneous reference angles, sufficient for reactive PI/PID tracking, the guidance law is extended to generate reference trajectories over the full prediction horizon, ensuring consistency between the guidance and DeePC layers. This predictive extension of ALOS is referred to as PALOS.

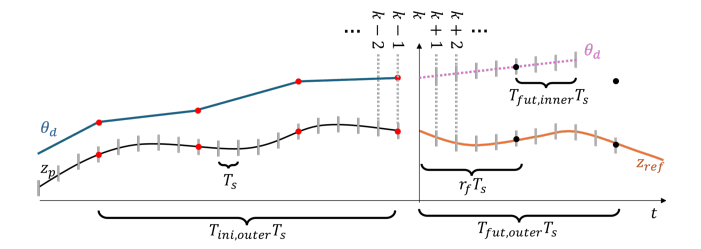


Fig. 3. Illustration of the sampled points (red and black dots) along the past and future trajectories from the outer loop to illustrate the reference trajectory generation for the inner control loop in pink via linear extrapolation.

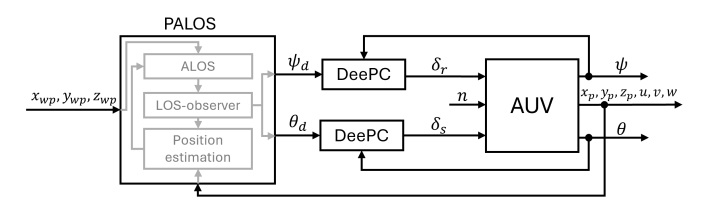


Fig. 4. Integration of PALOS into the DeePC framework for 3-D Path following.

7.1 Predictive ALOS

To construct a reference trajectory suitable for predictive control, the PALOS algorithm first computes the reference heading and pitch angles from the current AUV position, consistent with the standard ALOS formulation. These reference angles are then passed through the LOS observer to yield the initial desired commands for ψ_d and θ_d . For the computation of the further reference angles, the predictive guidance law assumes perfect tracking of the previously computed desired angles ψ_d and θ_d . Using the current AUV position (x_p, y_p, z_p) in the NED frame and the bodyframe velocities (u, v, w), the next predicted AUV position is computed assuming constant velocity throughout the prediction horizon as

$$\begin{bmatrix} x_{p,\text{next}} \\ y_{p,\text{next}} \\ z_{p,\text{next}} \end{bmatrix} = \begin{bmatrix} x_p \\ y_p \\ z_p \end{bmatrix} + h R(\phi, \theta_d, \psi_d) \begin{bmatrix} u \\ v \\ w \end{bmatrix}, \qquad (24)$$

where h denotes the sampling period and $R(\phi, \theta_d, \psi_d)$ is the rotation matrix transforming body-fixed velocities into the NED frame, defined in (A.2). At every further PALOS step within the prediction horizon, the estimated position is provided to the standard ALOS formulation to compute the next reference angles $(\psi_{\text{ref}}, \theta_{\text{ref}})$. These references are again passed through discrete-time LOS observers, which estimate both the filtered desired angles ψ_d and θ_d . The process is repeated iteratively, producing the reference trajectories for the DeePC optimization.

When an estimated position within the forward prediction horizon reaches the next waypoint, the active waypoint pair is updated accordingly. This ensures that the predicted reference trajectory anticipates upcoming path transitions, maintaining alignment with the intended spatial path across the entire prediction horizon. The integration of DeePC and PALOS with its own predictive loop is illustrated in Fig. 4

8. RESULTS

This section presents the simulation results obtained for the proposed DeePC-based control framework and compares its performance with the classical PI/PID control architecture across various scenarios, including nominal operation, external disturbances, nonlinear dynamic conditions and 3-D path following. For the classical architecture in all following scenarios, the best-performing PI/PID gains were selected from the preinitialized MSS toolbox for depth control and the tuning proposed in (Fossen, 2023) for heading control. The gain configuration of (Fossen and Aguiar, 2024) was also tested but yielded inferior performance. The PI/PID gains are as follows:

$$K_{p,\theta}=5.0, K_{i,\theta}=0.3, K_{d,\theta}=2.0, K_{p,\psi}=7.5,$$
 $K_{i,\psi}=0.75, K_{d,\psi}=15, K_{p,z}=0.1, K_{i,z}=1e-3$ For DeePC, the inner and outer control loops operated at frequencies of 20 Hz and 2 Hz, respectively, while for the PI/PID-based control, all loops operated at 20 Hz. The maximum possible angle for both, stern and rudder plane, are $\delta_{s,max}=\delta_{r,max}=\pm20^\circ$, while the maximum allowed pitch angle of the AUV is $\psi_{max}=\pm30^\circ$. These

The maximum possible angle for both, stern and rudder plane, are $\delta_{s,max} = \delta_{r,max} = \pm 20^{\circ}$, while the maximum allowed pitch angle of the AUV is $\psi_{max} = \pm 30^{\circ}$. These limitations were satisfied in the dynamic model via a saturation function and included in the DeePC framework as the regarding input and output constraints, as in (23).

8.1 General Control Performance

The PI/PID and DeePC-based controllers for heading and depth control are compared, with reference commands smoothed using the built-in LP filters of the MSS toolbox (Fossen and Perez, 2004). At $t=10\,\mathrm{s}$, a step command was applied toward a depth of 30 m and a heading of 60°. At $t=100\,\mathrm{s}$, a sinusoidal signal was superimposed on both reference trajectories to evaluate performance under more dynamic, albeit less realistic, reference variations. In both control approaches, the propeller speed was fixed to $n=1000\,\mathrm{rpm}$ during data collection and control execution. The specific DeePC hyperparameters (HP) are listed in Table 2.

Figure 5 illustrates a clear performance advantage of the DeePC controller, particularly in the heave control, due to its predictive nature in contrast to the reactive behavior of the PI/PID controller. This difference becomes especially evident when the sinusoidal reference is active, as the classical controller exhibits increased phase lag and tracking error. Quantitatively, the root-mean-square error (RMSE) values in Table 1 confirm the superior accuracy of the DeePC approach.

Remark: The different desired pitch angle references in Fig. 5 for DeePC and PI/PID result from the generation of those in the outer loop.

Analysis of the control inputs, i.e., the rudder and stern-plane commands δ_r and δ_s , respectively, reveals that the DeePC outputs exhibit abrupt changes at reference transitions. This behavior arises from the absence of modeled actuator dynamics in the employed AUV model. Incorporating these dynamics into the system model is therefore identified as a priority for future work to ensure physically realizable control signals. When data are collected from a real AUV, such actuator dynamics will naturally be embedded in the recorded sequences. The classical PI/PID controller, by contrast, produces smoother input transi-

Table 1. RMSEs for the yaw angle ψ , heave position z_p , and pitch angle θ regarding the given references for the different scenarios.

| | 8.1 | | 8.2 | | 8.3 | | 8.4 | |
|--------------------------|-------|------|---------------|------|-------|-------|-------|------|
| | DeePC | PID | ${\rm DeePC}$ | PID | DeePC | PID | DeePC | PID |
| ψ_{RMSE} (°) | 0.04 | | | | 0.07 | 0.7 | 0.29 | 1.17 |
| $z_{RMSE}\left(m\right)$ | 0.07 | 1.27 | 0.06 | 1.14 | 3.17 | 6.50 | - | - |
| θ_{RMSE} (°) | 0.18 | 0.62 | 0.13 | 0.54 | 9.60 | 33.71 | 0.04 | 0.24 |

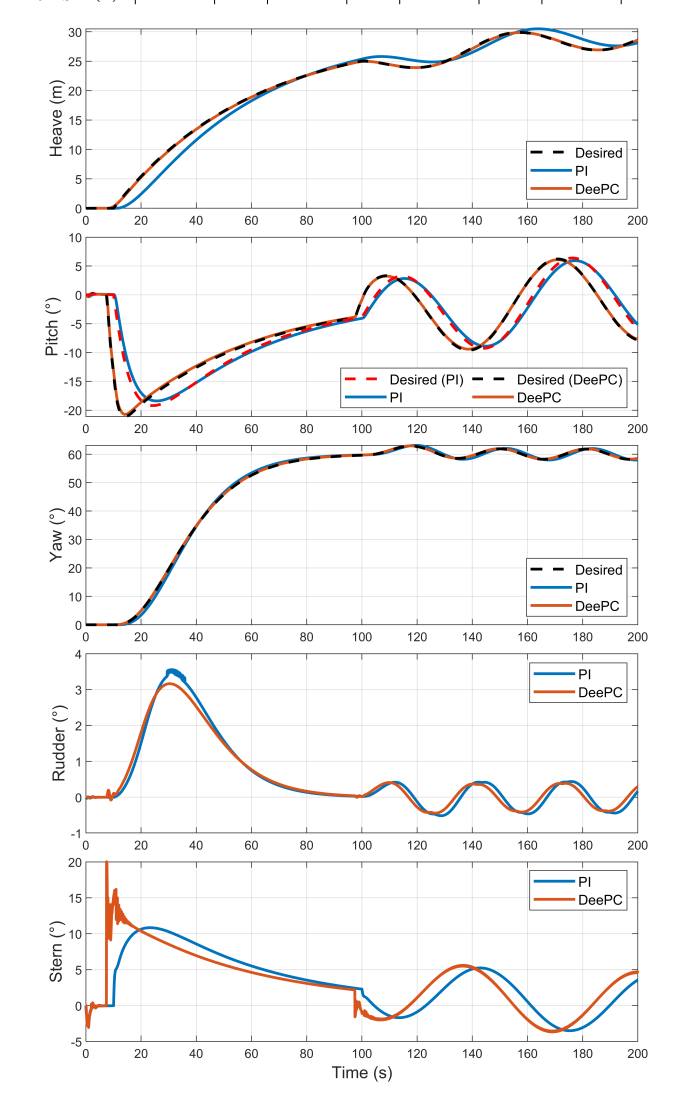


Fig. 5. Responses in heave position z_p , pitch angle θ , and yaw angle ψ of DeePC and PI/PID to each desired reference. Associated control command angles for the rudder plane and stern plane, δ_r and δ_s .

tions due to its inherent feedback structure and the LP filtering of the reference signals.

8.2 Robustness Evaluation under Ocean Currents

To assess the robustness of the proposed DeePC-based control architecture, a stress test was conducted by introducing ocean current disturbances modeled as described in Section 3.4. The horizontal current had a mean velocity magnitude of $V_c=0.5\,\mathrm{m/s}$ acting in the direction $\beta_{V_c}=150^\circ$ in the NED frame, while the vertical component was directed downward with $w_c=0.05\,\mathrm{m/s}$. To emulate small-scale turbulence, zero-mean Gaussian

perturbations were added at each time step to both the velocity and direction components of the current. Despite these relatively strong ocean currents, the DeePC controller exhibited consistently robust behavior, maintaining accurate trajectory tracking in both the heading and depth channels. Quantitatively, the RMSE values presented in Table 1 confirm the superior control performance under disturbances of the DeePC-based control compared to the conventional PI/PID architecture.

Remark: Due to the downward-directed current, the vertical disturbance supports reaching the smoothed step reference slightly faster, which results in a lower z_{RMSE} and θ_{RMSE} in Table 1, compared to Section 8.1.

8.3 Robustness Evaluation under Nonlinear Dynamics

To assess the robustness of the DeePC-based control architecture under nonlinear operating conditions, the AUV's propeller speed was systematically reduced, thereby decreasing the surge, sway, and heave velocities. Since the DeePC training data were collected at $n = 1000 \,\mathrm{rpm}$, this experiment effectively tests the controller's generalization capability beyond its data regime. As shown in the AUV modeling section, the vehicle's nonlinearities become most pronounced due to the velocities of the AUV. Generally, at reduced velocities, the AUV is physically unable to follow the reference profiles generated by the LP filter, as given in Fig.5. Consequently, the classical PI/PID controller exhibits significant integral wind-up, resulting in large overshoot, rendering the RMSE values inapplicable for fair comparison. Although anti-windup schemes could mitigate this issue, they were not implemented here to maintain methodological consistency. In contrast, the DeePC controller demonstrated strong robustness to these nonlinear effects. Despite transient tracking degradation when the vehicle momentarily lacked sufficient speed due to the decreased propeller speed, the controller successfully recovered and maintained trajectory tracking once the reference flattened and the AUV could catch up to the reference. The RMSE value reported in Table 1 corresponds to a propeller speed reduction to 700 rpm. Further testing showed that DeePC achieved stable and accurate control up to the maximum propeller speed of 1525 rpm and maintained satisfactory performance down to approximately 300 rpm when the reference step was appropriately scaled. Below 300 rpm, however, the nonlinearities exceeded the DeePC's depth-tracking capability. This operating point thus marks the observed nonlinearity-handling limit of the DeePC controller, which will be addressed in future work through adaptive or gain-scheduled extensions.

8.4 3-D Path following

The proposed PALOS combined with DeePC was evaluated for 3-D waypoint-based path following. For this setup, the propeller speed was fixed at $n=1000\,\mathrm{rpm}$, and the waypoint coordinates (x_{wp},y_{wp},z_{wp}) are listed in Fig. 6. The ocean current profile aligns with Sec. 8.2. The θ -DeePC controller employed more aggressive hyperparameters, as the inner loop receives a continuously updated reference in every control iteration, effectively eliminating stern-plane jitter and enabling more aggressive θ -DeePC. The corresponding HPs are summarized in Table 2. The PALOS-DeePC architecture achieved excellent

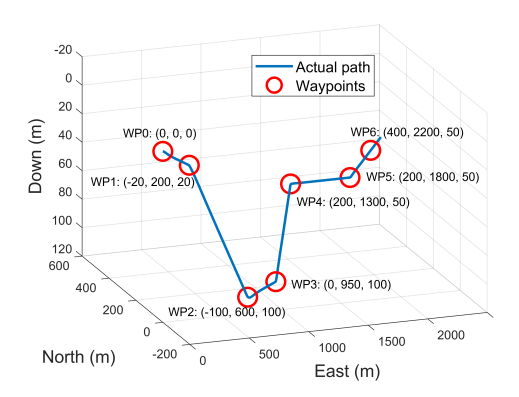


Fig. 6. 3-D path of the controlled AUV with desired waypoints in NED.

path-tracking performance, successfully reaching all waypoints as shown in the blue path of Fig. 6. Quantitative evaluation in Table 1 confirms its superior performance compared to the conventional ALOS-PI/PID combination. The main advantage arises at waypoint transitions, where the path direction changes abruptly. The ALOS-PI/PID control, being purely reactive, exhibits transient tracking errors during these path changes but recovers once the new path segment is reached again. In contrast, the predictive nature of PALOS-DeePC enables it to predict the upcoming transitions and adjust control actions preventive, maintaining accurate tracking even throughout the transitions. For a fairer comparison, smoothing the path transitions, e.g., by introducing spline-based connections between consecutive waypoints, would reduce the abruptness and improve the performance of ALOS-PI/PID. However, such a path design introduces additional complexity and tuning effort, while the PALOS-DeePC framework inherently handles these transitions within its predictive framework.

8.5 Hyperparameter

The DeePC HPs were tuned in a two-stage process to ensure robust performance across the AUV operating range. In the first stage, broad parameter intervals were explored, followed by a refined search in a second stage, as detailed in Appendix E. The selected HPs, summarized in Table 2, were chosen based on the RMSE and the smoothness of the control inputs. For the 3-D path-following case in Section 8.4, the θ -DeePC controller uses slightly modified weights, specifically Q=100 and R=100.

Table 2. Hyperparameters used for DeePC in the experiments.

| | T_{fut} | T_{ini} | T_d | λ_{ini} | λ_g | Q | R |
|----------|-----------|-----------|-------|-----------------|-------------|----------|----------|
| ψ | 10 | | | 10^{7} | | | |
| z_p | 7 | 7 | 200 | 10^{5} | 10^{2} | 10^{2} | 10^{3} |
| θ | 6 | 5 | 100 | 10^{7} | 10^{2} | 10^{4} | 500 |

9. CONCLUSION AND FURTHER WORK

This work successfully demonstrated DeePC for AUV control in both heading and depth regulation. A cascaded DeePC architecture was developed for depth control, incorporating a loop-frequency separation concept

that proved effective under disturbance and robustness tests. Furthermore, the PALOS algorithm was proposed and integrated with DeePC, enabling successful 3-D way-point path following of the REMUS 100 AUV. The results confirm that the proposed PALOS-DeePC approach constitutes a robust, data-driven, and predictive control solution, achieving high performance without requiring an explicit dynamic model and the associated effort. DeePC consistently outperformed the classical PI/PID control architecture, and although more aggressive gain tuning could narrow the performance gap, the predictive nature of DeePC inherently offers superior anticipatory behavior compared to reactive controllers.

Future work will extend the approach towards more nonlinear operation across the full speed range with gain-scheduled DeePC formulations, and advancing from waypoint-based path following to full trajectory tracking. Experimental validation on a real AUV would demonstrate the method's practical applicability.

Declaration of Generative AI and AI Technologies in the Writing Process: During the preparation of this work, the author(s) used ChatGPT in order to improve the grammar of this paper. After using this tool/service, the author(s) reviewed and edited the content as needed and take full responsibility for the content of the publication.

REFERENCES

Beard, R.W. and McLain, T.W. (2012). Autopilot Design Using Successive Loop Closure, 95–119. Princeton University Press.

Berberich, J. and Allgöwer, F. (2024). An overview of systems-theoretic guarantees in data-driven model predictive control. *Annual Review of Control, Robotics, and Autonomous Systems*, 8.

Berberich, J., Köhler, J., Müller, M.A., and Allgöwer, F. (2020). Data-driven model predictive control with stability and robustness guarantees. *IEEE Transactions on Automatic Control*, 66(4), 1702–1717.

Berberich, J., Köhler, J., Müller, M.A., and Allgöwer, F. (2021). Data-driven model predictive control: closed-loop guarantees and experimental results. at-Automatisierungstechnik, 69(7), 608–618.

Børhaug, E. and Pettersen, K.Y. (2006). Los path following for underactuated underwater vehicle. Elsevier IFAC Publications.

Breivik, M. and Fossen, T.I. (2009). Guidance laws for autonomous underwater vehicles. *Underwater vehicles*, 4, 51–76.

Coulson, J., Lygeros, J., and Dörfler, F. (2019). Dataenabled predictive control: In the shallows of the deepc. In 2019 18th European Control Conference (ECC), 307–312. IEEE.

Coulson, J., Lygeros, J., and Dörfler, F. (2021). Distributionally robust chance constrained data-enabled predictive control. *IEEE Transactions on Automatic Control*, 67(7), 3289–3304.

Coulson, J., Van Waarde, H.J., Lygeros, J., and Dörfler, F. (2022). A quantitative notion of persistency of excitation and the robust fundamental lemma. *IEEE Control Systems Letters*, 7, 1243–1248.

Elokda, E., Coulson, J., Beuchat, P.N., Lygeros, J., and Dörfler, F. (2021). Data-enabled predictive control for quadcopters. *International Journal of Robust and Nonlinear Control*, 31(18), 8916–8936.

- Faltinsen, O. (1993). Sea loads on ships and offshore structures, volume 1. Cambridge university press.
- Fossen, T.I. and Perez, T. (2004). Marine systems simulator (mss). https://github.com/cybergalactic/MSS. Accessed: 2025-10-14.
- Fossen, T.I. (2023). An adaptive line-of-sight (alos) guidance law for path following of aircraft and marine craft. *IEEE Transactions on Control Systems Technology*, 31(6), 2887–2894.
- Fossen, T.I. and Aguiar, A.P. (2024). A uniform semiglobal exponential stable adaptive line-of-sight (alos) guidance law for 3-d path following. *Automatica*, 163, 111556.
- Fossen, T. (2021). Handbook of Marine Craft Hydrodynamics and Motion Control, edition. John Wiley & Sons Inc.
- Gu, N., Wang, D., Peng, Z., Wang, J., and Han, Q.L. (2022). Advances in line-of-sight guidance for path following of autonomous marine vehicles: An overview. *IEEE Transactions on Systems, Man, and Cybernetics:* Systems, 53(1), 12–28.
- Huang, L., Zhen, J., Lygeros, J., and Dörfler, F. (2023). Robust data-enabled predictive control: Tractable formulations and performance guarantees. *IEEE Transactions on Automatic Control*, 68(5), 3163–3170.
- Imlay, F.H. (1961). The complete expressions for added mass of a rigid body moving in an ideal fluid. Technical report.
- Lamb, H. (1924). *Hydrodynamics*. University Press.
- Myring, D. (1976). A theoretical study of body drag in subcritical axisymmetric flow. *Aeronautical quarterly*, 27(3), 186–194.
- Rout, R. and Subudhi, B. (2020). Design of line-of-sight guidance law and a constrained optimal controller for an autonomous underwater vehicle. *IEEE Transactions on Circuits and Systems II: Express Briefs*, 68(1), 416–420.
- Shen, C. and Shi, Y. (2020). Distributed implementation of nonlinear model predictive control for auv trajectory tracking. *Automatica*, 115, 108863.
- Taubert, R., Eichhorn, M., Ament, C., Jacobi, M., Karimanzira, D., and Pfuetzenreuter, T. (2014). Model identification and controller parameter optimization for an autopilot design for autonomous underwater vehicles. In OCEANS 2014-TAIPEI, 1–9. IEEE.
- Willems, J.C., Rapisarda, P., Markovsky, I., and De Moor, B.L. (2005). A note on persistency of excitation. Systems & Control Letters, 54(4), 325–329.

Appendix A. ADDITIONAL NOTATION

To simplify the representation of the AUV dynamics, the state vector is expressed with respect to two coordinate systems: the North-East-Down (NED) frame and the body-fixed frame. Using the Euler angle transformation, the rotation matrix R_b^n defined in (A.2) transforms velocities from the body-fixed frame b to the NED frame n, as shown in (A.1) (Fossen, 2021), where v_n and v_b are velocities with respect to the NED and body-fixed frames respectively. The inverse matrix $R_n^b = (R_b^n)^{-1}$ enables the transformation in the opposite direction. Here, $c\psi$ and $s\psi$ denote the cosine and sine of the angle ψ , respectively.

$$R_b^n = \begin{bmatrix} c\psi c\theta & -s\psi c\phi + c\psi & s\theta & s\phi & s\psi & s\phi + c\psi c\phi & s\theta \\ s\psi c\theta & c\psi c\phi + s\phi & s\theta & s\psi & -c\psi & s\phi + s\theta & s\psi c\phi \\ -s\theta & c\theta & s\phi & c\theta c\phi \end{bmatrix}$$
(A.1)

The angular velocity mapping matrix T_k maps body angular velocities to Euler-angle rates.

$$T_{k} = \begin{bmatrix} 1 & \sin \phi \tan \theta & \cos \phi \tan \theta \\ 0 & \cos \phi & -\sin \phi \\ 0 & \sin \phi / \cos \theta & \cos \phi / \cos \theta \end{bmatrix}$$
(A.3)

The skew-symmetric matrix $S(r) \in \mathbb{R}^{3\times 3}$ associated with a vector $r = [r_x, r_y, r_z]^{\top}$ is defined as

$$S(r) = \begin{bmatrix} 0 & -r_z & r_y \\ r_z & 0 & -r_x \\ -r_y & r_x & 0 \end{bmatrix}.$$
 (A.4)

The system transformation matrix H(r), defined for a vector $r \in \mathbb{R}^3$, is given by (A.5), where $I_{3\times 3}$ is the identity matrix, $0_{3\times 3}$ is the zero matrix.

$$H(r) = \begin{bmatrix} I_{3\times3} & S(r)^{\top} \\ 0_{3\times3} & I_{3\times3} \end{bmatrix}$$
 (A.5)

$\begin{array}{cccc} {\rm Appendix~B.~PARAMETER~INTRODUCTION~FOR} \\ {\rm AUV~DYNAMIC~MATRICES} \end{array}$

Prior to describing the components of the 6-DOF rigidbody equations of motion, some fundamental concepts regarding the vehicle geometry must be established. The REMUS 100 AUV is represented using the Myring hull equations (Myring, 1976) and, in the MSS toolbox, approximated as a spheroid (Fossen and Perez, 2004). The spheroid is defined by its longitudinal, transverse, and vertical semi-axes a, b, and c. Owing to the near-cylindrical shape of the vehicle, the transverse and vertical semiaxes are equal (b = c), and the geometry satisfies the relation in (B.1) in terms of the AUV's length $L_{\rm AUV}$ and diameter D_{AUV} . To ensure consistency with the vehicle mass, a rescaling of the semi-axes is performed according to (B.2), where m is the vehicle mass and ρ the fluid density. Solving these relations yields the semi-axis values a and b defining the equivalent spheroidal representation of the REMUS 100.

$$\frac{L_{\rm AUV}^2}{a^2} + 2\frac{D_{\rm AUV}^2}{b^2} = 1 \tag{B.1}$$

$$m = \frac{4}{3}\pi\rho ab^2 \tag{B.2}$$

Using the semi-axes a and b of the spheroidal approximation, the moments of inertia about the body-fixed axes x_b , y_b , and z_b are computed according to (B.3)-(B.4).

$$I_{x_b} = \frac{2}{5}m b^2,$$
 (B.3)

$$I_{y_b} = I_{z_b} = \frac{1}{5}m(a^2 + b^2),$$
 (B.4)

The vectors $r_{bG}, r_{bB} \in \mathbb{R}^3$ denote the positions of the vehicle's center of gravity and buoyancy relative to the body-fixed origin. Using the transformation matrix H(r) in (A.5), forces and moments can be mapped between frames shifted by these vectors.

To estimate the added system inertia matrix the factors α_0 and β_0 with eccentricity e needs to be introduced:

$$e = 1 - \left(\frac{b}{a}\right)^2 \tag{B.5}$$

$$\alpha_0 = \frac{2(1-e^2)}{e^3} \left(\frac{1}{2} \ln \frac{1+e}{1-e} - e\right)$$
 (B.6)

$$\beta_0 = \frac{1}{e^2} - \frac{1 - e^2}{2e^3} \ln \frac{1 + e}{1 - e}$$
 (B.7)

Following the k-factors introduced in (Lamb, 1924), the added-mass contributions to the system inertia can be estimated. The factors are defined as

$$k_{1} = \frac{\alpha_{0}}{2 - \alpha_{0}}, \quad k_{2} = \frac{\beta_{0}}{2 - \beta_{0}},$$

$$k' = \frac{e^{4}(\beta_{0} - \alpha_{0})}{(2 - e^{2})(2e^{2} - (2 - e^{2})(\beta_{0} - \alpha_{0}))},$$
(B.8)

yielding the diagonal added-mass matrix

$$M_A = -\operatorname{diag}\{X_{\dot{u}}, Y_{\dot{v}}, Z_{\dot{w}}, K_{\dot{p}}, M_{\dot{q}}, N_{\dot{r}}\}$$

$$= \operatorname{diag}\{mk_1, mk_2, mk_2, r_{44}I_x, k'I_y, k'I_y\}.$$
(B.9)

While classical hydrodynamics predicts zero added moment in roll (element (4,4) of M_A) for a spheroidal hull (Imlay, 1961), practical vehicles such as the RE-MUS 100 experience additional hydrodynamic contributions from the control surfaces and the propeller. Accordingly, this roll-related entry of the added-mass matrix is nonzero, $M_A(4,4) = r_{44}I_x$, capturing these effects in the simulation (Fossen and Perez, 2004).

The relative speed U_r given in (B.10) is defined as the Euclidean norm of the body-fixed linear velocity components of the AUV relative to the surrounding water, while the relative horizontal and vertical speeds, U_{rh} and U_{rv} respectively, are defined as in (B.11).

$$U_r = \sqrt{u_r^2 + v_r^2 + w_r^2} \tag{B.10}$$

$$U_{rh} = \sqrt{u_r^2 + v_r^2}, \quad U_{rv} = \sqrt{u_r^2 + w_r^2}$$
 (B.11)

The vehicle's orientation relative to the oncoming flow can be characterized by the angle of attack α and the sideslip angle β , defined in terms of the relative velocity components as

$$\alpha = \tan^{-1} \left(\frac{w_r}{u_r} \right), \qquad \beta = \sin^{-1} \left(\frac{v_r}{U_r} \right).$$
 (B.12)

Appendix C. THE AUV DYNAMIC MATRICES

The kinematic component of the 6-DOF rigid-body equations of motion for the AUV, given in (4), is defined by the transformation matrix $J(\eta)$. This matrix maps body-fixed linear and angular velocities to the time derivatives of the vehicle's position and orientation in the NED frame, as detailed in (C.1). It is constructed from the rotation

matrix in (A.2) and the angular velocity transformation matrix in (A.3).

$$J(\eta) = \begin{bmatrix} R_b^n(\phi, \theta, \psi) & 0_{3\times 3} \\ 0_{3\times 3} & T_k(\phi, \theta, \psi) \end{bmatrix}$$
 (C.1)

The inertia matrix M of the AUV is composed of the rigid-body inertia M_{RB} and the added-mass matrix M_A . The term M_{RB} depends on the vehicle's mass properties and is expressed through the transformation matrix H from (A.5), defined with respect to the center of gravity vector r_{bG} . The hydrodynamic contribution M_A , introduced in (B.9), accounts for the added inertia caused by the acceleration of the surrounding fluid.

$$M_{\mathrm{RB}} = H^{\top}(r_{\mathrm{bg}}) \operatorname{diag} \{m, m, m, I_{x_b}, I_{y_b}, I_{z_b}\} H(r_{\mathrm{bg}})$$
(C.2)

In the MSS toolbox, M_A is assumed constant, resulting in a constant M. The REMUS 100 exhibits both port–starboard and fore–aft symmetry, which simplifies the inertia representation according to Fossen (2021) to the sparse structured form shown in (C.3).

$$M = M_{RB} + M_A = \begin{bmatrix} m_{11} & 0 & 0 & 0 & m_{15} & 0 \\ 0 & m_{22} & 0 & m_{24} & 0 & 0 \\ 0 & 0 & m_{33} & 0 & 0 & 0 \\ 0 & m_{42} & 0 & m_{44} & 0 & 0 \\ m_{51} & 0 & 0 & 0 & m_{55} & 0 \\ 0 & 0 & 0 & 0 & 0 & m_{66} \end{bmatrix}. \quad (C.3)$$

The Coriolis–centripetal matrix $C(\nu_r)$ represents gyroscopic and cross-coupling effects arising from linear and angular motion. It is composed of the rigid-body term $C_{RB}(\nu_r)$ and the added-mass term $C_A(\nu_r)$ as

$$C(\nu_r) = C_{RB}(\nu_r) + C_A(\nu_r). \tag{C.4}$$

The rigid-body part $C_{RB}(\nu_r)$ is derived from M_{RB} and depends on the angular velocities, while $C_A(\nu_r)$ depends on the relative linear velocities.

$$C_{\mathrm{RB}}\left(v_{\mathrm{r}}\right) = H^{\top}\left(r_{\mathrm{bg}}\right) \begin{bmatrix} 0 & -mr & mq & 0 & 0 & 0 \\ mr & 0 & -mp & 0 & 0 & 0 \\ -mq & mp & 0 & 0 & 0 & 0 \\ 0 & 0 & 0 & 0 & I_{z}r & -I_{y}q \\ 0 & 0 & 0 & -I_{z}r & 0 & I_{x}p \\ 0 & 0 & 0 & I_{y}q & -I_{x}p & 0 \end{bmatrix} H\left(r_{\mathrm{bg}}\right) \tag{C.:}$$

$$C_{\mathcal{A}}(v_r) = \begin{bmatrix} 0 & 0 & 0 & 0 & -Z_{\dot{w}}w_r & Y_{\dot{v}}v_r \\ 0 & 0 & 0 & Z_{\dot{w}}w_r & 0 & -X_{\dot{w}}u_r \\ 0 & 0 & 0 & -Y_{\dot{v}}v_r & X_{\dot{w}}u_r & 0 \\ 0 & -Z_{\dot{w}}w_r & Y_{\dot{v}}v_r & 0 & -N_{\dot{r}}r & M_{\dot{q}}q \\ Z_{\dot{w}}w_r & 0 & -X_{\dot{w}}u_r & N_{\dot{r}}r & 0 & -K_{\dot{p}}p \\ -Y_{\dot{v}}v_r & X_{\dot{w}}u_r & 0 & -M_{\dot{q}}q & K_pp & 0 \end{bmatrix}$$
(C.6)

The damping matrix $D(\nu_r)$ is modeled as a diagonal matrix, representing proportional damping in each degree of freedom. To account for nonlinear effects at higher speeds, the damping in the surge and sway directions decreases exponentially with the total relative velocity U_r defined in (B.10), introducing velocity-dependent behavior in the damping matrix. The resulting formulation is

$$D(\nu_r) = - \, \mathrm{diag} \, \Big\{ \, X_u e^{-3U_r}, \; Y_v e^{-3U_r}, \; Z_w, \; K_p, \; M_q, \; N_r \, \Big\}. \quad \mbox{(C.7)} \label{eq:D}$$

Each damping coefficient is related to the corresponding element of the inertia matrix parameterized by a characteristic time constant T_i , assuming first-order linear damping dynamics:

$$\begin{split} X_u &= -\frac{m_{11}}{T_1}, \quad Y_v = -\frac{m_{22}}{T_2}, \quad Z_w = -\frac{m_{33}}{T_3}, \\ K_p &= -\frac{m_{44}}{T_4}, \quad M_q = -\frac{m_{55}}{T_5}, \quad N_r = -\frac{m_{66}}{T_6}. \end{split} \tag{C.8}$$

The vector $g(\eta)$ represents the restoring forces and moments acting on the vehicle due to gravity and buoyancy, resulting in nonlinear attitude-dependent behavior. For neutrally buoyant underwater vehicles such as the RE-MUS 100, these effects are primarily determined by the position of the center of gravity, defined as $r_{bG} = [x_g, y_g, z_g]^T$ and the gravitational force mg, relative to the body-fixed origin as in (C.9).

$$g(\eta) = \begin{bmatrix} 0 \\ 0 \\ 0 \\ z_{\rm g} mg \cos(\theta) \sin(\phi) - y_{\rm g} mg \cos(\theta) \cos(\phi) \\ z_{\rm g} mg \sin(\theta) + x_{\rm g} mg \cos(\theta) \cos(\phi) \\ x_{\rm g} mg \cos(\theta) \sin(\phi) - y_{\rm g} mg \sin(\theta) \end{bmatrix}$$
(C.9)

The restoring forces and moments depend only on roll and pitch angles, as these determine the orientation of the vehicle relative to the vertical gravity and buoyancy forces. The yaw rotation ψ does not influence the restoring effects, since it represents a rotation about the gravity vector itself.

With the control input vector $u = [\delta_s, \delta_r, n_p]^{\top}$ containing the stern and rudder plane angles, and propeller speed, the generalized forces and moments τ acting on the AUV can be generated. The rudder and stern planes generate drag forces along the surge direction,

$$X_r = -\frac{1}{2}\rho U_{rh}^2 A_r C_{L_{\delta_r}} \delta_r^2, \quad X_s = -\frac{1}{2}\rho U_{rv}^2 A_s C_{L_{\delta_s}} \delta_s^2,$$
(C.10)

as well as lift forces in sway and heave, respectively,

$$Y_r = -\frac{1}{2}\rho U_{rh}^2 A_r C_{L_{\delta_r}} \delta_r, \quad Z_s = -\frac{1}{2}\rho U_{rv}^2 A_s C_{L_{\delta_s}} \delta_s,$$
(C.11)

where ρ is the water density, A_r and A_s are the rudder and stern-plane areas, δ_r , δ_s are their deflection angles, and the relative horizontal and vertical speeds, U_{rh} and U_{rv} , are given in (B.11). For positive propeller shaft speeds $n_p \geq 0$, the propeller thrust X_{prop} and torque K_{prop} can be expressed in simplified form as

$$X_{\text{prop}} = \alpha_X n_p^2 + \beta_X n_p, \quad K_{\text{prop}} = \alpha_K n_p^2 + \beta_K n_p, \quad (C.12)$$

where the coefficients α_X , β_X , α_K , and β_K collect the effects of fluid density, propeller and plane geometrics, advance-ratio scheduling, deduction factors, and the thrust/torque coefficients.

The resulting generalized force vector is given in (C.13), where x_r , x_s are the longitudinal positions of the rudder and stern planes relative to the body-fixed origin.

$$\tau = [X_{\text{prop}} + X_r + X_s, Y_r, Z_s, K_{\text{prop}}, -x_s Z_s, x_r Y_r]^{\top}$$
(C.13)

The lift and drag forces are modeled as functions of the angle of attack α , given in (B.12), using the corresponding lift and drag coefficients $C_L(\alpha)$ and $C_D(\alpha)$. The resulting magnitudes are given in (C.14), where S is the vehicle's reference surface area.

$$F_{\text{lift}} = \frac{1}{2} \rho U_r^2 \, S \, C_L(\alpha), \qquad F_{\text{drag}} = \frac{1}{2} \rho U_r^2 \, S \, C_D(\alpha),$$
(C.14)

The forces are resolved into the body-fixed coordinate system by rotation with the angle of attack α , yielding the longitudinal and vertical components

$$\tau_{LD,X} = -F_{\text{drag}} \cos \alpha + F_{\text{lift}} \sin \alpha,$$

$$\tau_{LD,Z} = -F_{\text{drag}} \sin \alpha - F_{\text{lift}} \cos \alpha.$$
 (C.15)

The lift-drag vector τ_{LD} is then expressed in (C.16) assuming that no side force or rotational moments arise from these components.

$$\tau_{LD} = [\tau_{LD,X}, 0, \tau_{LD,Z}, 0, 0, 0]^{\top}$$
 (C.16)

The cross-flow drag forces and moments are modeled following the strip-theory formulation by Faltinsen (1993) and Fossen (2021). The AUV hull is approximated as a series of two-dimensional strips of draft $T = D_{AUV}$ and length $L = L_{AUV}$, each experiencing a local flow velocity dependent on the sway and heave components (v_r, w_r) and the corresponding angular rates (r, q). The sectional drag is characterized by the two-dimensional drag coefficient $C_{\rm d}^{\rm 2D}(v_r, w_r)$, yielding the cross-flow drag integrals in (C.17). The total generalized cross-flow drag vector acting on the vehicle is given in (C.18), representing the hydrodynamic forces and moments in sway, heave, pitch, and yaw due to lateral and vertical flow separation along the hull.

$$\begin{split} Y_{CF} &= -\frac{1}{2} \rho T C_{\rm d}^{\rm 2D}(v_r, w_r) \int_{-\frac{L}{2}}^{\frac{L}{2}} |v_r + xr| \left(v_r + xr\right) {\rm d}x, \\ Z_{CF} &= -\frac{1}{2} \rho T C_{\rm d}^{\rm 2D}(v_r, w_r) \int_{-\frac{L}{2}}^{\frac{L}{2}} |w_r + xq| \left(w_r + xq\right) {\rm d}x, \\ M_{CF} &= -\frac{1}{2} \rho T C_{\rm d}^{\rm 2D}(v_r, w_r) \int_{-\frac{L}{2}}^{\frac{L}{2}} x \left|v_r + xr\right| \left(v_r + xr\right) {\rm d}x, \\ N_{CF} &= -\frac{1}{2} \rho T C_{\rm d}^{\rm 2D}(v_r, w_r) \int_{-\frac{L}{2}}^{\frac{L}{2}} x \left|w_r + xq\right| \left(w_r + xq\right) {\rm d}x. \\ \tau_{CF} &= \left[0, Y_{CF}, Z_{CF}, 0, M_{CF}, N_{CF}\right]^{\top}, \end{split} \tag{C.18}$$

Appendix D. OCEAN CURRENT MODEL

The current velocity expressed in the body-fixed frame is defined as

$$\nu_{c} = [u_{c}, v_{c}, w_{c}, p_{c}, q_{c}, r_{c}]^{\top}$$
 (D.1)

 $\nu_c = \left[u_c, v_c, w_c, p_c, q_c, r_c\right]^\top. \tag{D.1}$ The first three components (u_c, v_c, w_c) represent the linear ocean current velocity, while the remaining components (p_c, q_c, r_c) correspond to rotational current effects. Under the common assumption of irrotational ocean flow, these angular components are negligible and simplify to (D.2).

$$\nu_c^b = \left[u_c, v_c, w_c \right]^\top. \tag{D.2}$$

To obtain ν_c^b , the ocean current defined in the NED frame must be transformed using the standard coordinate transformation of (A.1), as expressed in (D.4). The current in the NED frame, ν_c^n , is represented as a superposition of a horizontal component of magnitude V_c and a vertical component W_c . The horizontal flow direction is specified by the angle β_c , while, due to the separation of components, the vertical current is assumed to act strictly along the z-axis, leading to (D.3).

$$\nu_c^n = [V_c \cos(\beta_c) , V_c \sin(\beta_c) , W_c]^{\top}$$

$$\nu_c^b = (R_b^n)^{-1} \nu_c^n.$$
(D.3)

$$\nu_a^b = (R_b^n)^{-1} \nu_a^n.$$
 (D.4)

Reformulating (5) into an explicit differential form yields (D.5), which expresses the dynamics in terms of the time derivatives of the vehicle velocity $\dot{\nu}$ and the ocean current velocity $\dot{\nu}_c$:

$$\dot{\nu}_r = \dot{\nu} - \dot{\nu}_c = M^{-1} (\tau + \tau_{LD} + \tau_{CF} - C(\nu_r) \nu_r - D(\nu_r) \nu_r - g(\eta)).$$
(D.5)

To obtain $\dot{\nu}$, which represents the actual acceleration of the vehicle and is the primary quantity of interest, the derivative of the ocean current velocity $\dot{\nu}_c^b$ must be computed using the skew-symmetric matrix defined in (A.4). Substituting (D.6) into (D.5) enables the evaluation of $\dot{\nu}$, completing the formulation of the current-compensated dynamic model.

$$\dot{\nu}_c^b = -S \begin{pmatrix} p \\ q \\ r \end{pmatrix} \begin{bmatrix} u_c \\ v_c \\ w_c \end{bmatrix} = \begin{bmatrix} rv_c - qw_c \\ -ru_c + pw_c \\ qu_c - pv_c \end{bmatrix}. \tag{D.6}$$

Appendix E. HYPERPARAMETER TUNING PROCEDURE

The DeePC HPs were tuned through a structured twostage process to ensure robust performance across the full operating range of the AUV. In the first stage, broad parameter ranges were explored in an approximate search, where each HP was varied individually while the others were held constant. The resulting preliminary values formed the basis for the second stage, in which each HP was re-evaluated separately through ten independent simulations per candidate value—five under nominal conditions and five with external disturbances (ocean currents), due to the stochastic variability of the PRBS used for data collection. Different reference trajectories were applied across the repetitions to ensure robustness over the full operational range. Each trajectory contained an LPsmoothened step reference that was superimposed with a sinusoidal component, comparable to Fig. 5. The bestperforming value was selected manually based on the RMSE of the overall tracking performance and qualitative assessment of control-input smoothness. Across all HPs, the control performance "valley" was relatively flat and with a wide region of near-optimal values. Consequently, the final parameter set was chosen from within this region, prioritizing control smoothness over minor numerical differences in RMSE.